Energy & Environmental Science

PAPER

View Article Online
View Journal | View Issue

Cite this: *Energy Environ. Sci.*, 2017, **10**, 2180

A triboelectric generator based on self-poled Nylon-11 nanowires fabricated by gas-flow assisted template wetting†‡

Yeon Sik Choi, Qingshen Jing, Anuja Datta, Chess Boughey and Sohini Kar-Narayan*

Triboelectric generators have emerged as potential candidates for mechanical energy harvesting, relying on motion-generated surface charge transfer between materials with different electron affinities. In this regard, synthetic organic materials with strong electron-donating tendencies are far less common than their electron-accepting counterparts. Nylons are notable exceptions, with odd-numbered Nylons such as Nylon-11, exhibiting electric polarisation that could further enhance the surface charge density crucial to triboelectric generator performance. However, the fabrication of Nylon-11 in the required polarised δ′-phase typically requires extremely rapid crystallisation, such as melt-quenching, as well as "poling" *via* mechanical stretching and/or large electric fields for dipolar alignment. Here, we propose an alternative one-step, near room-temperature fabrication method, namely gas-flow assisted nano-template (GANT) infiltration, by which highly crystalline "self-poled" δ′-phase Nylon-11 nanowires are grown from solution within nanoporous anodised aluminium oxide (AAO) templates. Our gas-flow assisted method allows for controlled crystallisation of the δ′-phase of Nylon-11 through rapid solvent evaporation and an artificially generated extreme temperature gradient within the nanopores of the AAO template, as accurately predicted by finite-element simulations. Furthermore, preferential crystal orientation originating from template-induced nano-confinement effects leads to self-poled δ′-phase Nylon-11 nanowires with higher surface charge distribution than melt-quenched Nylon-11 films, as observed by Kelvin probe force microscopy (KPFM). Correspondingly, a triboelectric nanogenerator (TENG) device based on as-grown templated Nylon-11 nanowires fabricated *via* GANT infiltration showed a ten-fold increase in output power density as compared to an aluminium-based triboelectric generator, when subjected to identical mechanical excitations.

Received 11th May 2017,
Accepted 9th August 2017

DOI: 10.1039/c7ee01292f

rsc.li/ees

Broader context

Energy harvesting from ubiquitous ambient vibrations represents a viable energy solution for the rapidly increasing number of low-power autonomous, wireless, portable and wearable electronic devices. Triboelectric generators have recently generated tremendous interest in this regard as they are capable of converting mechanical energy from the relative motion of two dissimilar materials into useful electricity, based on contact electrification and electrostatic induction arising from the materials having different electron affinities. In order to achieve high levels of energy harvesting performance, materials with electron-donating tendencies must be paired with those with electron-accepting tendencies. The bulk of the literature focuses on the latter, as these typically include materials that are easier to synthesise. Nylon-11 belongs to the less-explored family of synthetic and organic electron-donating materials, although the crystalline phase required for superior triboelectric performance has remained elusive in the bulk due to the typically harsh processing conditions. We therefore demonstrate a novel fabrication method by which Nylon-11 nanowires of the required crystalline phase can be achieved with controlled precision, using a simple one-step gas-flow assisted template wetting approach. We show that our Nylon-11 nanowires exhibit remarkable triboelectric properties, including inherent electrical polarization, which leads to enhanced energy harvesting performance.

Department of Materials Science and Metallurgy, University of Cambridge, 27 Charles Babbage Road, Cambridge CB3 0FS, UK. E-mail: sk568@cam.ac.uk

† Electronic supplementary information (ESI) available. See DOI: 10.1039/c7ee01292f

‡ Supporting data for this paper is available at the DSpace@Cambridge data repository (https://doi.org/10.17863/CAM.12537).

Introduction

The rapidly growing demand for energy solutions for autonomous, wireless, portable and wearable electronic devices has prompted great interest in environment-friendly energy harvesting devices.

In this respect, harvesting energy from ubiquitous mechanical vibrations can provide a viable power solution for these devices, such as wireless sensors that may be implanted within the body for healthcare monitoring, or embedded within structures for early fault detection.[1] Mechanical-to-electrical conversion can be achieved *via* electrostatic and electromagnetic generators, as well as through piezoelectric materials.[1,2] A more recent approach has been through the use of triboelectric generators based on contact electrification and electrostatic induction between materials having dissimilar electron affinities.[3,4] If two materials with different electron affinities make contact, the resulting charge transfer causes the material which gains charge to become negatively charged, and the other material which loses charge becomes positively charged; a phenomenon known as contact electrification. When the two materials are separated, if there is no conducting path between the two surfaces, then these surfaces are able to maintain their induced charges as static electricity; this process is called electrostatic induction. A periodic potential difference can thus be generated across the materials as a result of a periodic relative motion between the two. Maximising the surface area over which the charge transfer takes place enhances the effect, and thus several nanostructuring routes have been adopted to achieve this, resulting in many different kinds of triboelectric "nanogenerators" (TENGs) that have been reported over the past few years.[5–9]

For an efficient triboelectric generator, the appropriate pairing of materials is critical, and versions of empirical "triboelectric series" have enabled such selection through careful consideration of the positions of different materials with respect to one another.[3,10,11] Although the sequence of this triboelectric series can be affected by many variables, such as electron affinity, surface structure, and dielectric permittivity *etc.*, materials on the positive and negative series tend to consist of negatively charged and positively charged molecules, respectively.[12,13] As a result, triboelectric generators based on pairs of materials located on the extreme opposite ends of the triboelectric series are expected to show superior mechanical energy harvesting capability. Interestingly, the majority of the research till date has almost exclusively focused on tribo-negative materials, in other words, electron-accepting materials, such as polytetrafluoroethylene (PTFE).[4] These have been paired with aluminium or copper as the tribo-positive or electron-donating counterpart, even though these metals are not located on the extreme positive end of the triboelectric series, as shown in Fig. 1a. This is because the vast majority of materials on the positive side of the triboelectric series are biological or natural materials, such as human skin and cotton, and have relatively low mechanical stiffness and/or shape controllability.[14] Nylon, however, is a notable exception among tribo-positive materials, being synthetic in nature with excellent mechanical properties that allow for easy control of its shape and subsequent integration into triboelectric generators. Therefore, an investigation into Nylon as a potential tribo-positive candidate is essential to enhance triboelectric performance and extend the range of triboelectric generator applications.

There have been a few reports where Nylon has been used as a tribo-positive material,[15–17] but these studies have focused on even-numbered Nylons, such as Nylon-6 or Nylon-66, with only slightly better output performance than other tribo-positive materials such as silk or aluminium that have been reported.[18] In this work, we instead focus on odd-numbered Nylons, such as Nylon-11, that exhibit ferroelectric properties because of the dipole orientation resulting from the arrangement of polyamide molecules within adjacent chains, similar to more well-known ferroelectric polymers such as poly(vinylidene fluoride) (PVDF) and its copolymers.[2,19–21] Compared to these fluorinated polymers, Nylon-11 shows a similar degree of ferroelectric properties, such as

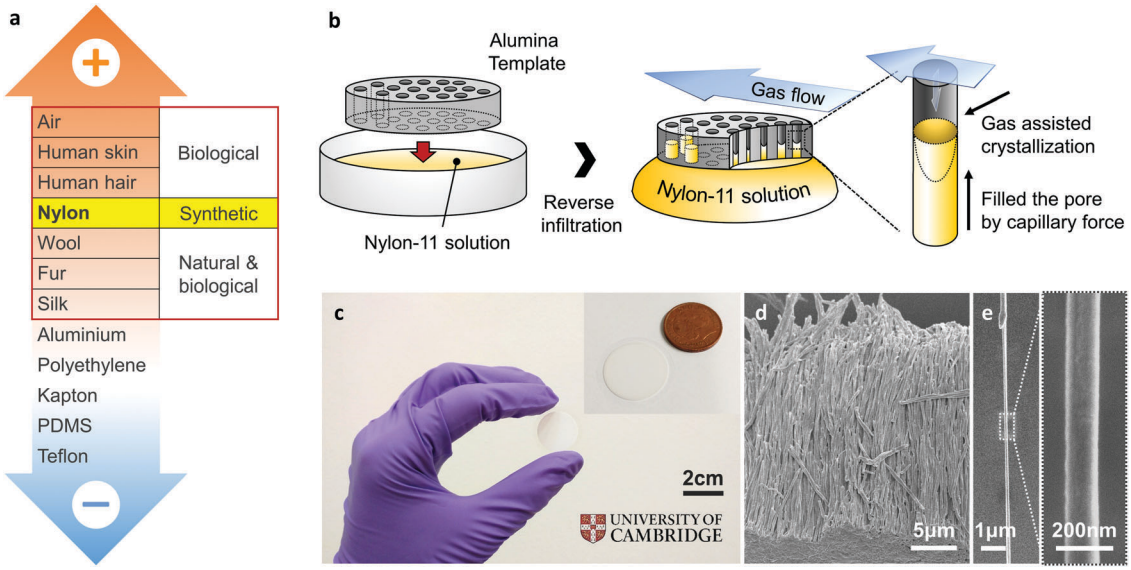

Fig. 1 (a) Triboelectric series of common materials with highlighted position of tribo-positive materials. (b) Schematic of the nanowire fabrication procedure. (c) Photographs of a fabricated nanowire-filled AAO template. The inset shows size comparison with a British one-pence coin. (d and e) SEM images of template-freed nanowires and a single strand of Nylon nanowire, respectively.

dipole moment[22] and piezoelectric coefficient,[23] with the added advantage of higher thermal stability.[24,25]

The effect of remnant polarisation in the performance of TENG devices based on ferroelectric polymers has been previously studied, whereby a high voltage was applied across the polymer to achieve dipolar alignment along the direction of the applied field. According to these studies, positively poled PVDF and its copolymer films showed more than double the power output when incorporated into triboelectric generators as compared to the un-poled film.[17,26] This is due to an increase in surface charge density as a result of the remnant polarisation.[27] These studies indicate that poled Nylon-11 may be well-suited for triboelectric applications through inherent surface charge density modification. However, in order to maximise the required polarisation property of this material, extreme processing conditions are required, including mechanical stretching and/or electrical poling process under high voltage ($\sim$140 MV m^{-1}), which are major processing issues that need to be overcome.

In order to realise maximum polarisation in Nylon-11, the material needs to possess a pseudo-hexagonal structure with randomly oriented hydrogen bonds, referred to as the "δ′-phase" (ESI,† S1), where this structure allows for easy aligning of the dipole moment.[28,29] This δ′-phase, however, is typically achieved through extremely fast crystallisation that is required to avoid the formation of large domain size.[30–33] As a result, most of the studies regarding the δ′-phase Nylon-11 have been carried out on films grown *via* melt-quenching. Although several alternative techniques, such as spin coating,[34] vapour deposition,[35] electrospinning,[36] thermal annealing,[37] and adding carbon nanostructures,[38] have been suggested, most of these reported approaches resulted in a lower crystallinity and/or still require harsh processing conditions, such as high temperature (290 °C) and high voltage (40 kV). Moreover, these methods involve further drawing and electrical poling process to enhance the remnant polarisation of the Nylon-11 films.[23]

Here, we propose an alternative one-step, near room-temperature method, namely gas-flow assisted nano-template (GANT) infiltration method, for the fabrication of highly crystalline "self-poled" δ′-phase Nylon-11 nanowires within nanoporous anodised aluminium oxide (AAO) templates, without any subsequent processing such as stretching and/or poling required. The gas-flow assisted method allows for controlled crystallisation rate that manifests as a combination of rapid solvent evaporation and an extreme temperature gradient within the nanopores of the template, as accurately predicted by finite-element simulations, resulting in the δ′-phase crystal structure. Furthermore, the preferential crystal orientation originating from template-induced nano-confinement effects lead to self-polarization of the nanowires, increasing average crystallinity up to $\sim$40%. The self-poled δ′-phase Nylon-11 nanowires show enhanced surface charge distribution when compared to melt-quenched films as observed by Kelvin probe force microscopy (KPFM). Correspondingly, a TENG device based on GANT Nylon-11 nanowires showed a ten-fold increase in output power density compared to an aluminium-based triboelectric generator, when subjected to identical mechanical excitations.

Results and discussion

Remnant polarisation in our as-grown Nylon-11 nanowires, without the need of subsequent stretching and/or high-voltage poling, is achieved *via* nano-confinement during the template wetting process.[39–41] This method has been shown to enable self-poling of a ferroelectric polymer through grapho-epitaxial alignment in the lamellae.[20,25,41,42] Recent work from our group has shown that the template-induced nanoconfinement led to self-poling in poly(vinylidene difluoride–trifluoroethylene) (P(VDF-TrFE)) nanowires[20] as well as Nylon-11 nanowires,[25] resulting in a highly efficient piezoelectric nanogenerators.[41] However, controlling the exact crystal structure through nano-confinement methods remains challenging, in part owing to the crystal growth initiation site. For a typical template-wetting process where a polymer melt or solution is introduced into the top surface of the template *via* spin coating, nucleation is initiated from the surface of the bulk solution and propagated into the nano-sized pores.[43] Such bulk-initiated nucleation and growth mechanism imposes restrictions on the control of polymer crystal structure, due to the difficulties in controlling the rate of crystallisation. We mitigate this problem by using a reverse template infiltration technique with assisted gas flow. Capillary forces allow the target solution to infiltrate from the bottom, directly exposing the solution to air. Furthermore, assisted gas-flow enables precise control of the crystallisation rate of the Nylon-11 polymer solution, resulting in the required δ′-phase crystal structure. We note that this phase was not prominent in the XRD diffraction pattern reported in our previous work[25] where a more typical template-wetting method was employed. We find that the strong presence of the δ′-phase in Nylon-11 nanowires leads to enhanced surface polarisation, and thus precise control of this crystalline phase through our GANT method is crucial to triboelectric energy harvesting performance.

The GANT fabrication procedure is schematically illustrated in Fig. 1b. To achieve δ′-phase Nylon-11 nanowires, the AAO template was placed on top of a 17. 5 wt% Nylon-11 solution in formic acid at 70 °C. At the same time, assisted gas flow ($\sim$3 m s^{-1}) was introduced in a direction parallel to the template surface. Fig. 1c shows a photograph of an AAO template (diameter $\sim$2 cm and thickness $\sim$60 μm) filled with Nylon-11 nanowires grown using the GANT method. High-resolution scanning electron microscope (SEM) imaging (FEI Nova Nano SEM) was carried out on the resulting nanowires. Stretched and entangled Nylon-11 nanowire strands (white thread-like regions) were observed in cross-sectional SEM images of a cleaved template (ESI,† Fig. S2). The observed deformation of the nanowires was a result of the template cleaving process. In contrast, well-aligned nanowire arrays were detected in samples after the template material was dissolved using mild acid (see Methods section) (Fig. 1d). A single nanowire strand has uniform width and length of 200 nm and 60 μm respectively, which are similar to the dimensions of the AAO template pore channels (Fig. 1e).

Gas-flow assisted crystal structure control

Detailed crystal structural characterization was subsequently carried out by X-ray diffraction (XRD, Bruker D8). At room

temperature, a melt-quenched film with pseudo-hexagonal δ′-phase typically showed broader reflection peak at $2\theta \sim 21.6^\circ$ corresponding to (*hk*0) plane, which is merged planes of (100), (010), and (110).[44] However, without assisted gas-flow, Nylon-11 nanowires displayed a relatively strong peak at $2\theta = 22.6^\circ$ with a very weak δ′-phase peak ($2\theta = 21.6^\circ$) (Fig. 2a). This diffraction pattern is consistent with our previous result regarding the Nylon-11 nanowire manufactured by conventional template wetting method.[25] The GANT infiltration process allowed control of the crystal structure, wherein we were able to manipulate the rate of crystallisation by adjusting the speed of gas flow. As shown in Fig. 2a (left panel), the relative peak intensity of the δ′-phase gradually increased with increasing the rate of assisted gas-flow up to a gas-flow rate of ~ 3 m s^{-1}, without any further increment thereafter. The relative changes in intensities between the peak at 21.6° and peak at 22.6° are depicted in Fig. 2a (right panel), where the variation in average peak intensities is plotted as a function of gas flow rate. This result indicates that the crystal structure of nano-confined Nylon-11 nanowires could be well-controlled using different gas-flow rate, leading to the formation of pseudo-hexagonal δ′-phase Nylon-11 nanowires. It should be noted that there exists some confusion about the distinction between γ and δ-phase of Nylon-11. Based on the recent work of Pepin *et al.*, we identify the δ′-phase in our Nylon-11 nanowires which has the required polar characteristics.[44] (see ESI,† S1). The crystalline phase corresponding to the 22.6° peak is less straightforward to identify as it has not been reported in the literature, though a possible explanation may be that this peak corresponds to the (210/010) plane of triclinic α′ phase.

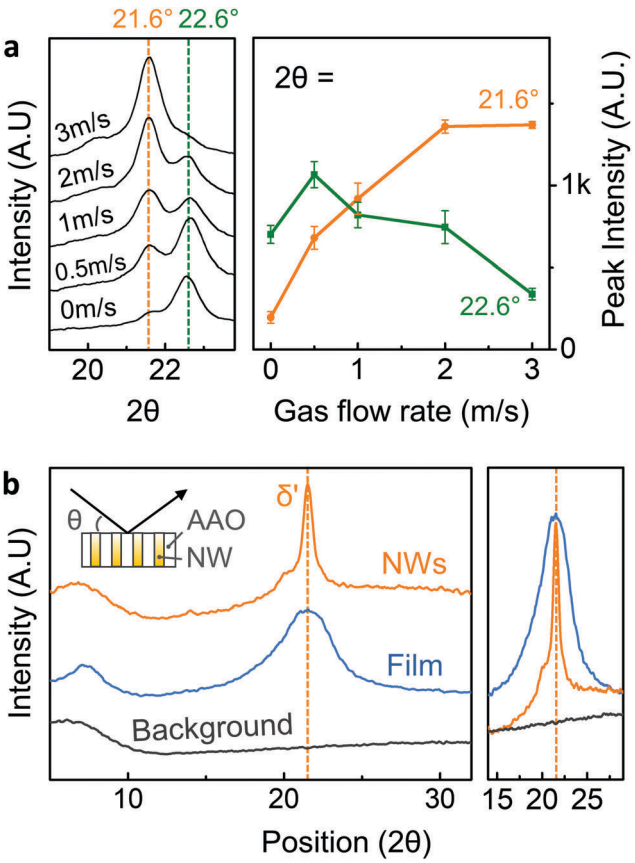

Fig. 2 (a) (left) XRD patterns of nanowire-filled templates crystallised at various assisted gas-flow rates. (right) Based on the normalised XRD patterns, the average intensity of the peak at 21.6° and 22.6° is plotted as a function of assisted-gas flow rate. (b) XRD patterns of a nanowire-filled template (orange), melt-quenched film (blue), and silicon background (grey). The right image shows the magnification of the δ′-phase range.

In order to compare the crystallography of the nanowires, melt quenched Nylon-11 films with δ′-phase, were fabricated. Fig. 2b shows the XRD from both a melt-quenched film and nanowires in the AAO template. While the melt-quenched film showed a relatively broad δ′-phase peak at $2\theta_{hk0} = 21.6^\circ$, the δ′-phase nanowires that were grown using the GANT method exhibited a δ′-phase peak with small full width at half-maximum. It means that the smectic-like phase has more organised (pseudo)-hexagonal lattice structure.[44] It is to be noted that the volume of nanowires was only about $\sim 50\%$ of the film with the same size and thickness (ESI,† Fig. S3) as the XRD data for nanowires was taken while the nanowires were still embedded in the AAO template. This indicated that the actual amount of crystalline region in the nanowire per unit area is larger than that of the melt-quenched film. These results suggest that even through the conventional melt-quenching method, the presence of large amorphous regions cannot be prevented in the films due to the thickness of the film and the low thermal conductivity of Nylon.[33] However, this problem is mitigated *via* the GANT method where the δ′-phase in Nylon-11 nanowires is realised to a larger extent.

The crystallisation mechanism initiated by the GANT method was verified using finite element analysis using COMSOL Multiphysics as illustrated in Fig. 3, and ESI,† Fig. S4. To further investigate the rapid crystallisation process, the effect of both solvent evaporation as well as temperature gradient within the solution have been considered. In terms of solvent evaporation, our simulations revealed that through the assisted gas-flow, the artificially generated dry and cool turbulent air flow effectively encourages the evaporation of the solvent. Fig. 3a and b shows the induced turbulent flow by assisted gas within the nanopore channels, whose speed increased with increasing assisted gas-flow velocity (Fig. 3c). The velocity of the turbulent gas flow, evaluated 10 nm above the surface of the solution, was 36 μm s^{-1} for an assisted-gas velocity of 3.1 m s^{-1}. This is an extremely high flow rate considering the nanopore is ~ 200 nm in diameter. As a result, nucleation can be initiated at the surface of the exposed solution by rapid solvent evaporation. In our computational model, we also considered the effect of solution cooling within the pore channel: both turbulent flow-induced evaporative cooling and conductive cooling *via* the nano-template pore walls. The overall cooling mechanism is demonstrated in Fig. 3d and e, taking into consideration the turbulent flow around the exposed Nylon solution, as well as the heat transfer through the pore walls. As a result of this cooling, a temperature gradient is generated both on the top surface and the side of the Nylon solution. Fig. 3f shows the significant temperature gradient produced by evaporative cooling (orange) and thermal conduction (blue) as a function of the distance from the top and

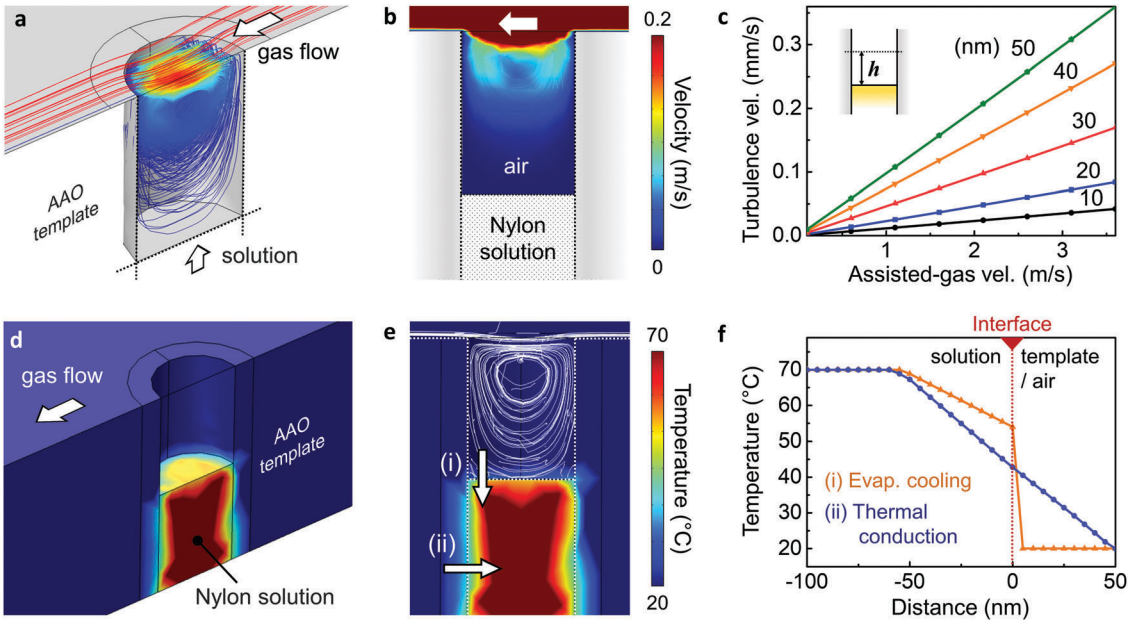

Fig. 3 Numerical simulation results of turbulence flow generated by assisted gas-flow (3.1 m s^{-1}): (a) 3D view and (b) *xz*-plane view. (c) Plot showing the relationship between the velocity of turbulent flow at different heights above the solution surface and assisted gas-flow rate. (d) Simulation result of heat transfer around the solution-filled nano-pore. (e) The *xz*-plane view of (d) with turbulent flow showing two dominant cooling mechanisms: (i) evaporative cooling and (ii) thermal conductive cooling. (f) The temperature gradient from the centre of the solution to the air (orange) and template wall (blue). The initial temperature of the Nylon solution and assisted gas were taken to be 70 °C and 20 °C, respectively.

side surfaces of the solution, respectively. The crystal growth direction can be inferred from these heat transfer simulation, as the growth of the crystalline region is most likely to occur in the direction of the largest temperature gradient (ESI,† Fig. S6). In addition, considering the crystal growth direction of the GANT method and due to the size of the nano-pores, the crystal growth size (~100 nm) can be limited, resulting in extremely rapid nucleation and growth. Hence fast crystallisation is achieved within the confines of the nanopores, even with mild external conditions, such as low gas flow rate (3 m s^{-1}) and near-room temperature conditions.

Self-poled δ′-phase nanowires through GANT method

Differential scanning calorimetry (DSC) was carried out to determine the thermal and structural properties of our Nylon-11 nanowires as shown in Fig. 4a, from which the melting temperature T_m and the melt crystallisation temperature T_c were recorded. To investigate the crystal ordering effect within the template pores, as-received melt-quenched films, stretched melt-quenched films and template-freed nanowire mats were also prepared. During the heating cycle, a single melting peak at 190 °C was observed in the melt-quenched film (black) corresponding to the δ′-phase crystal formation.[34,44] In contrast, a significant change in T_m was noted from the additionally stretched film (blue) as compared to the non-stretched film. The stretched film showed a dominant melting peak at 184.5 °C with a minor melting peak (190 °C), with an increase in crystallinity from 29% to 40% (ESI,† Fig. S7).[32] Both the formation of a new low-temperature melting peak and improved crystallinity may indicate the additionally aligned molecular chain structure developed by the mechanical stretching process.[45] During the cooling cycle, similar to the melting point shift described above, we found that stretched films crystallise at higher temperatures (162 °C) compared to the non-stretched film (158 °C) due to a more ordered crystal structure. The thermal properties of the nanowires can be explained on the basis of several factors: nanowire size effect, nano-template effect and crystal ordering effect. Both nanowires within the template (orange), as well as those freed from the template (green) displayed double melting behaviour. The additional low temperature melting peak can be explained by nanoscale size effect. According to the Gibbs-Thomson equation,[46,47] the melting point depression δT_m is given by

$$\Delta T_m = T_m - T_m(d) = 4\sigma_{sl}T_m/(d\Delta H_f\rho_s)$$

where T_m is the normal (bulk) melting point, $T_m(d)$ is the melting point of crystals of size d, σ_{sl} is the surface tension of the solid–liquid interface, d is particle size, ΔH_f is the bulk enthalpy of fusion (per g of material), and ρ_s is the density of the solid.[46] It means that the melting point of the nanowires was depressed due to the nano-confined structure and surface tension of the Nylon-11/template interface. From nanowires in the template (orange), the dominant melting peak was observed at a lower temperature (185 °C), as compared to the template-freed nanowires (green) which displayed dominant melting peaks at a higher temperature (190 °C). This is because, in the case of nanowires within the AAO template, both the very thin nanowire diameter as well as the surface tension between Nylon-11 and the nano-template interface affect the melting behaviour.[46] In the cooling cycle, the nano-template effect was confirmed by the relatively broader crystallization temperature

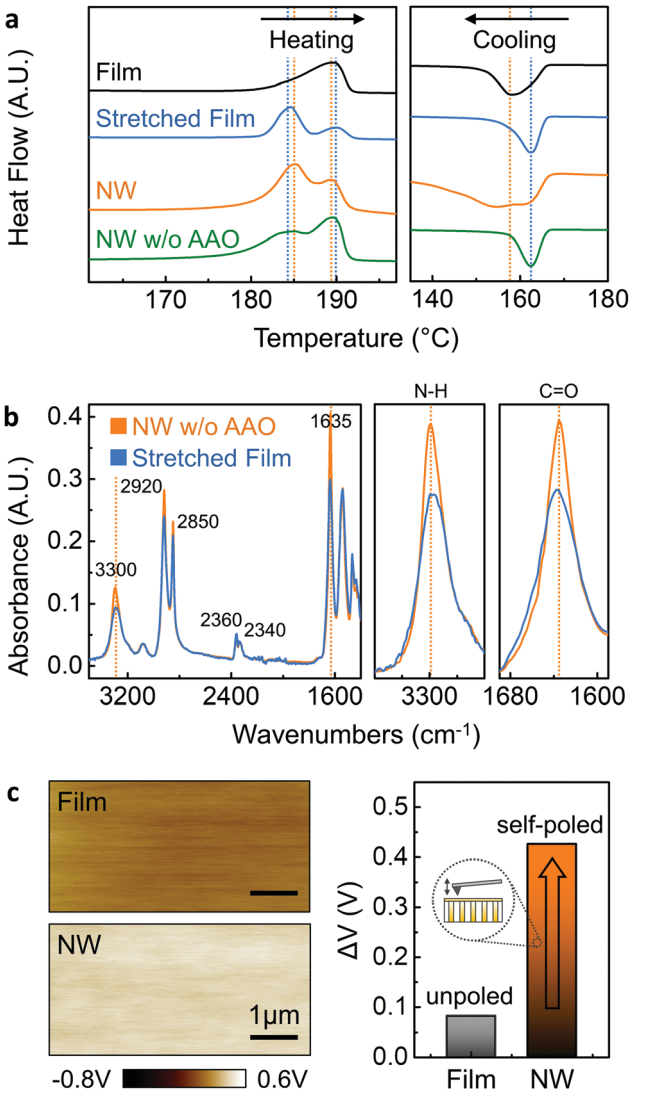

Fig. 4 (a) DSC thermograms for the melt-quenched film (black), additionally stretched film (blue), nanowires inside the template (orange), and template freed nanowires (green). (b) FT-IR absorbance spectra for template-freed nanowires (orange) and additionally stretched film (blue). (c) (left) KPFM potential images of the melt-quenched Nylon-11 film and the top surface of the self-poled nanowires filled template device. (right) The plot for the surface charge potential difference of each sample. The inset shows KPFM measured surface structure.

of the nanowire in the template. Thermal behaviour of template-freed nanowires, however, makes us infer an additional effect that influences the property of the nanowires. This is because cooling behaviour of template-freed nanowires (green) and stretched film (blue) are substantially similar and have the same T_c (162 °C). In addition, the δ′-phase nanowires displayed much higher degree of crystallinity (39%) than those of the melt-quenched film (29%).[33,48] The crystallinity of the δ′-phase nanowire is rather similar with those of stretched film (40%), even though the nano-confined structure showed much lower latent heat of fusion ΔH_m.[47] All of these phenomena suggests that, during the GANT process, δ′-phase nanowires were likely to have experienced crystalline ordering. Similar to the molecular alignment from the film-drawing process, grapho-epitaxial alignment originating from the nanotemplate-pore walls resulted in highly ordered structure, giving rise to similarities in the thermal behaviour and high crystallinity observed in the stretched film. Our results indicate that the GANT method successfully enabled highly ordered δ′-phase nanowires to be formed without additional drawing process.

The molecular bond structure of δ′-phase nanowires was measured using room temperature Fourier transform infrared (FT-IR) spectroscopy (Fig. 4b). A template freed δ′-phase nanowire mat (orange) and stretched film (blue) were prepared to confirm the preferential crystal orientation originating from nano-confinement. For more detailed analysis, the direction of the infrared spectra for drawing should be considered since the peak intensity can be changed depending on the chain alignment in the draw direction.[49] Considering the drawing direction, parallel and perpendicular direction infrared absorption spectra were measured from δ′-phase nanowires and stretched film, respectively (ESI,† Fig. S8). According to the literature, FT-IR spectra of Nylon-11 have two important regions related to dipole alignment. The region 1500–1700 cm^{-1} contains the amide I and II mode and is assigned to hydrogen-bonded or free amide group. The band at 3300 cm^{-1} (amide A peak) is assigned to N–H stretching vibration and is sensitive to the hydrogen bond.[31,34,50] The region 1500–1700 cm^{-1} is shown in Fig. 4b for both stretched film and nanowires, containing the amide I and amide II bands. In this region, two materials show similar intensity except for 1635 cm^{-1} band because the conformation in the amorphous phase is expected to be the same.[34] The 2920 and 2850 cm^{-1} bands of both materials are assigned to the antisymmetric and symmetric CH_2 stretching modes of the methylene groups, respectively. The significant differences in the absorption intensities of the N–H stretching modes at 3300 cm^{-1} and C═O stretching modes at 1635 cm^{-1} show direct evidence for the self-polarization in the nanowires. The parallel direction absorbance peak in the template-freed nanowire mat was found to be higher for both bands compared to the perpendicular direction peak intensity of the stretched film. Considering the relatively higher peak intensity in the perpendicular direction spectra and peak intensity rise in the parallel spectra due to the electric poling process,[29,49] the higher intensity of the nanowire mat suggests that nanowires obtained from the GANT method have preferential crystal orientation.

In order to investigate the direction of polarization and quantify the surface charge variations between Nylon-11 nanowires and melt-quenched films arising from the self-poled nature of the former, we employed Kelvin probe force microscopy (KPFM), where the surface charge potential difference between the material and an atomic force microscope (AFM) tip can be measured (Fig. 4c). Melt-quenched Nylon-11 film showed a surface potential difference of 82 mV. In contrast, the higher surface potential (426 mV) was observed from the self-poled δ′-phase nanowire-filled template. Furthermore, the enhanced surface charge potential difference of self-poled nanowires demonstrates the relationship between polarisation and surface charge density. Our results indicate an "upward"

direction of polarisation, which corresponds to the expected charge donating property.

Nylon-11 nanowire based TENG device

A TENG device was fabricated using self-poled nanowires embedded within AAO template. The bottom side of AAO template was coated by gold (Au) electrodes (~100 nm), and an Au-coated Teflon film was prepared as a counterpart substrate. Aluminium (Al) films and melt-quenched Nylon-11 film were also prepared to compare the device performance with the nanowire-based TENG. Fig. 5a and b show the open-circuit voltage (V_{OC}) and short-circuit current density (J_{SC}) respectively, measured in response to the periodic impacting at a frequency (f) of 5 Hz and amplitude of 0.5 mm in an energy harvesting setup that has been previously described.[41] The aluminium-based triboelectric generator showed a peak V_{OC} of ~40 V and a peak J_{SC} of ~13 mA m^{-2}. Following the triboelectric series, higher TENG performance was observed from a melt-quenched Nylon-11 film-based triboelectric generator with V_{OC} of ~62 V and J_{SC} of ~21 mA m^{-2} than from the aluminium-based triboelectric generator. The self-poled Nylon-11 nanowire based TENG displayed further enhanced output performance with a peak V_{OC} of ~110 V and a peak J_{SC} of ~38 mA m^{-2} likely due to the self-poled nature of the nanowires. We conducted analytical simulations using a finite element method (FEM) with COMSOL Multiphysics software to further confirm the effects of self-polarization on triboelectric potential (ESI,† Fig. S9). As expected, when compared with aluminium and Nylon-film based triboelectric generators, higher triboelectric potential was obtained from the self-poled Nylon nanowire-based TENG since the self-poled nanowires increased the charge density (σ) on the electrified surfaces.

The electrical power output of the triboelectric generators was measured across different resistors. The peak output power density of 1.03 W m^{-2}, 0.19 W m^{-2}, and 0.099 W m^{-2} were observed from the Nylon-11 nanowire, Nylon-11 (melt-quenched) film, and aluminium based device respectively under impedance-matched conditions at a load resistance of ~20 MΩ (Fig. 5c and ESI,† Fig. S10). The observed output power from the nanowire based TENG was ~6 times and ~10 times higher than those of a melt-quenched Nylon-11 film and aluminium-based triboelectric generators, respectively. Such remarkable improvement in the output performance of δ′-phase nanowires can be rationalised as follows; the self-polarization of the nanowires gave rise to larger surface charge density, which resulted in more charges being transferred as compared to the film surface. It should be noted that the surface area of the nanowires is only ~50% as compared to the melt-quenched film. It indicates that polarisation in the nanowire effectively further enhances the surface charge density of the device. The electrical output was found to increase with increasing impact frequencies and amplitudes (ESI,† Fig. S11). In addition, fatigue testing was carried out by continuously impacting the device for up to 30 hours at 5 Hz (≈540 000 cycles). Fig. S12a (ESI†) shows that the Nylon-11 nanowire-based TENG device exhibited negligible change in output current density over the entire period of continuous testing. Reliability tests under various humidity conditions were also carried out by impacting the Nylon-11 nanowire based TENG device within a humidity-controlled box (ESI,† Fig. S12b). Although Nylon is known to be prone to degradation in the presence of moisture, the Nylon-11 nanowire-based TENG showed reliable output performance up to

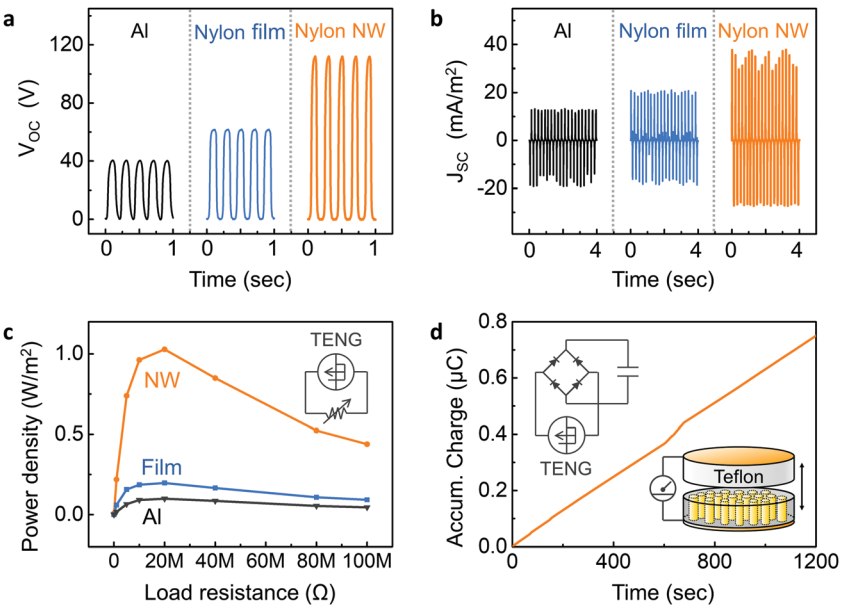

Fig. 5 (a) Open-circuit output voltages of triboelectric generators with different combinations of materials. The output voltage increases from ~40 V in the device with aluminium to ~110 V in the device with δ′-phase Nylon nanowires. (b) Short-circuit output current densities of the same devices as in (a). (c) The power density of different triboelectric generators as a function of variable load resistance. (d) Charge accumulation of the nanowire-based TENG with respect to time. Left top and right bottom insets show the circuit structure and schematic of the TENG.

high humidity condition (~80%), indicating that the AAO template serves to encapsulate and protect the nanowires from environmental factors.

To further confirm the effect of self-polarization on TENG devices, we also measured the output performance of the template-free nanowire mat where the nanowires are lying on the substrate with randomly oriented polarisation directions (ESI,† Fig. S13a–c). Interestingly, the template-freed nanowire mat-based TENG device generated suppressed output performance (V_{OC} = 20 V and J_{SC} = 4.0 mA m^{-2}), even though it was thinner and had a larger effective surface area (ESI,† Fig. S13d and e). Due to the randomly oriented polarisation in the nanowire mat, the generation of triboelectric charges was likely inhibited during the contact and separation process. These results support the orientation directed polarisation effects in the Nylon-11 nanowires while they are still aligned and embedded within the template.

To confirm the energy generated by the δ′-phase nanowires, a 470 μF capacitor was connected to the device using a full-wave bridge rectifying circuit. The Nylon nanowire-based TENG subjected to low-level oscillating mechanical pressure at 5 Hz for about 20 minutes successfully charged the capacitor with a charging speed of ~38 μC min^{-1}. Notably, the accumulated charge increased with time as shown in Fig. 5d, suggesting the Nylon-11 nanowire-based TENG had excellent stability. The electric power produced by the Nylon-11 nanowire-based TENG was used to directly turn on several commercial light-emitting diodes (LEDs). During contact and separation with 5 Hz frequency, 36 white LEDs were driven by the produced output voltage without the need for external energy storage devices (ESI,† Fig. S14).

Experimental

Fabrication of Nylon-11 nanowires

Calculated wt% Nylon-11 (Sigma-Aldrich, [–NH(CH$_2$)$_{10}$CO–]$_n$) solutions were prepared in the solvent formic acid (Sigma-Aldrich, Reagent grade ≥95%) at 70 °C. When observing the nanowires using the GANT method, 25 mm diameter AAO templates (Anopore, Whatman) with a diameter of 200 nm and thickness of 60 μm were placed on an 800 μL Nylon-11 solution droplet. To control the crystallisation rate of solution, assisted gas (air) flow was introduced upon the AAO template using a portable mini fan placed immediately next to the floating template. The rate of assisted gas was controlled by fan rotation speed and measured by an anemometer. The whole drying experiment proceeded under room temperature. Detailed descriptions of the nanowire preparation set-up and treatment were reported previously.[25] To obtain the Nylon-11 nanowire arrayed mats, we immersed the nanowire-filled AAO template in a 40 vol% phosphoric acid solution for 4 h.

Fabrication of Nylon-11 films

Nylon-11 films were produced by quenching the molten film (210 °C) into an ice bath. In the case of stretched films, quenched films were drawn to a draw ratio of 3 at room temperature.

Characterization

The Nylon-11 nanowires were visualised using field-emission scanning electron microscopy (FE-SEM, FEI Nova Nano SEM). The crystal phase and crystalline quality of the Nylon-11 nanowires inside the AAO template and Nylon-11 films were measured using an X-ray diffraction (XRD) machine (Bruker D8) using Cu Kα radiation (λ = 1.5418 Å) with a background silicon substrate. Numerical modelling of gas flow, heat transfer around nanopores, and the triboelectric effect were achieved by COMSOL Multiphysics. For simulation details see ESI.† Differential scanning calorimeter (DSC) was carried out using TA Instruments Q2000 DSC at a scanning rate of 5 °C per minute. Around 2 mg of samples was used and sealed into T zero aluminium DSC pans. Fourier transform infrared (FTIR) was performed using a Bruker Tensor 27 IR spectrometer in the reflection mode. Kelvin probe force microscopy (KPFM) measurements were carried out using Bruker Multimode 8 with Antimony (n) doped Si (tip radius <35 nm, resonance frequency 150 kHz). AC voltages were applied from a lock-in amplifier. Film thickness was measured by stylus surface profilometer (Veeco Dektak 6 M). To study the electrical output performance of triboelectric generators, a bespoke energy harvesting measurement setup[41] was utilised, recording the output open-circuit voltage (V_{OC}) and short-circuit current (I_{SC}) by a multimeter (Keithley 2002) and a picoammeter (Keithley 6487), respectively. In the present work, an impacting frequency of 5 Hz with an amplitude of ~1 mm was used. 24 μm thick Aluminum film and 60 μm thick melt-quenched Nylon-11 film with the same diameter (~2 cm) were prepared to compare the triboelectric generator performance with the nanowire-based TENG. To make the TENG device, one side of the Nylon-11 NW filled AAO template and the melt-quenched film was coated by sputter coating ~100 nm thick Au (using k550 Emitech) layer.

Conclusions

To summarise, we have demonstrated for the first time, a novel and facile gas-flow assisted nano-template (GANT) infiltration method for the fabrication of highly oriented, self-poled δ′-phase Nylon-11 nanowires, as a rarely synthesised tribo-positive material. Assisted gas-flow controlled the crystallisation speed, resulting in the δ′-phase crystal structure. Preferential crystal orientation originated from the nanoconfinement effect in the template, resulting in self-poling of the Nylon-11 nanowires with an increased average crystallinity of up to ~40%. When self-poled Nylon-11 nanowires were combined with counterpart tribo-negative surfaces, such as Teflon, the resulting output power was observed to be ~6 times and ~10 times higher than that of melt-quenched Nylon-11 film and aluminium based triboelectric generators, respectively. The output power generated by the Nylon-11 nanowire-based TENG device was high enough to drive commercial electronic components such as LEDs and capacitors without external power sources. The work provides a new strategy to develop highly crystalline and self-poled Nylon in a facile and robust manner, thus providing a means to realise a

much-needed synthetic tribo-positive material with enhanced surface charge density for use in high-performance triboelectric generators.

Author contributions

Y. S. C. fabricated the materials and devices and carried out the experimental work and computational modelling. S. K.-N. designed and guided the experimental work. A. D. provided guidance on the fabrication aspects while Q. J. provided guidance on the modelling aspects of the paper as well as device design. C. B. helped with the energy harvesting measurements. Y. S. C. and S. K.-N. co-wrote the paper. All authors discussed the results and commented on the paper. All authors have given their approval to the final version of the manuscript.

Conflicts of interest

There are no conflicts to declare.

Acknowledgements

This work was financially supported by a grant from the European Research Council through an ERC Starting Grant (Grant no. ERC-2014-STG-639526, NANOGEN). S. K.-N., Y. S. C. and A. D. are grateful for financial support from this same grant. Y. S. C. is grateful for studentship funding through the Cambridge Commonwealth, European & International Trust. Q. J. is grateful for financial support through a Marie Sklodowska Curie Fellowship, H2020-MSCAIF-2015-702868. CB thanks the EPSRC Cambridge NanoDTC, EP/G037221/1, for studentship funding. The authors thank Dr Thomas Bennett for discussions.

References

1 K. A. Cook-Chennault, N. Thambi and A. M. Sastry, *Smart Mater. Struct.*, 2008, **17**, 43001.
2 S. Crossley, R. A. Whiter and S. Kar-Narayan, *Mater. Sci. Technol.*, 2014, **30**, 1613–1624.
3 Z. L. Wang, *ACS Nano*, 2013, **7**, 9533–9557.
4 Z. L. Wang, J. Chen and L. Lin, *Energy Environ. Sci.*, 2015, **8**, 2250–2282.
5 F. R. Fan, Z. Q. Tian and Z. Lin Wang, *Nano Energy*, 2012, **1**, 328–334.
6 G. Zhu, Z. Lin, Q. Jing, P. Bai, C. Pan, Y. Yang and Y. Zhou, *Nano Lett.*, 2013, **13**, 847.
7 G. Cheng, Z. Lin, L. Lin, Z. Du and Z. L. Wang, *ACS Nano*, 2013, **7**, 7383–7391.
8 C. K. Jeong, K. M. Baek, S. Niu, T. W. Nam, Y. H. Hur, D. Y. Park, G. Hwang, M. Byun, Z. L. Wang, Y. S. Jung and K. J. Lee, *Nano Lett.*, 2014, **14**, 7031–7038.
9 H. Kang, H. Kim, S. Kim, H. J. Shin, S. Cheon, J. H. Huh, D. Y. Lee, S. Lee, S. W. Kim and J. H. Cho, *Adv. Funct. Mater.*, 2016, **26**, 7717–7724.
10 J. Henniker, *Nature*, 1962, **196**, 474.
11 G. Zhu, C. Pan, W. Guo, C. Y. Chen, Y. Zhou, R. Yu and Z. L. Wang, *Nano Lett.*, 2012, **12**, 4960–4965.
12 S. Shin, Y. H. Kwon, Y. Kim, J. Jung, M. H. Lee and J. Nah, *ACS Nano*, 2015, **9**, 4621–4627.
13 S. Shin, Y. E. Bae, H. K. Moon, J. Kim, S. Choi and Y. Kim, *ACS Nano*, 2017, **11**, 6131–6138.
14 H. J. Kim, J. H. Kim, K. W. Jun, J. H. Kim, W. C. Seung, O. H. Kwon, J. Y. Park, S. W. Kim and I. K. Oh, *Adv. Energy Mater.*, 2016, **6**, 1–6.
15 T. Zhou, C. Zhang, C. B. Han, F. R. Fan, W. Tang and Z. L. Wang, *ACS Appl. Mater. Interfaces*, 2014, **6**, 14695–14701.
16 Y. Zheng, L. Cheng, M. Yuan, Z. Wang, L. Zhang, Y. Qin and T. Jing, *Nanoscale*, 2014, **6**, 7842–7846.
17 J.-H. Lee, R. Hinchet, T. Y. Kim, H. Ryu, W. Seung, H.-J. Yoon and S.-W. Kim, *Adv. Mater.*, 2015, **27**, 5553–5558.
18 X. Pu, M. Liu, X. Chen, J. Sun, C. Du, Y. Zhang, J. Zhai, W. Hu and Z. L. Wang, *Sci. Adv.*, 2017, **3**, e1700015.
19 A. J. Lovinger, *Science*, 1983, **220**, 1115–1121.
20 R. A. Whiter, Y. Calahorra, C. Ou and S. Kar-Narayan, *Macromol. Mater. Eng.*, 2016, **301**, 1016–1025.
21 Y. S. Choi, J. Sung, S. J. Kang, S. H. Cho, I. Hwang, S. K. Hwang, J. Huh, H. Kim, S. Bauer and C. Park, *Adv. Funct. Mater.*, 2012, 1–9.
22 J. W. Lee, Y. Takase, B. A. Newman and J. I. Scheinbeim, *J. Polym. Sci., Part B: Polym. Phys.*, 1991, **29**, 279–286.
23 B. A. Newman, P. Chen, K. D. Pae and J. I. Scheinbeim, *J. Appl. Phys.*, 1980, **51**, 5161–5164.
24 Y. Takase, J. W. Lee, J. I. Scheinbeim and B. A. Newman, *Macromolecules*, 1991, **24**, 6644–6652.
25 A. Datta, Y. S. Choi, E. Chalmers, C. Ou and S. Kar-Narayan, *Adv. Funct. Mater.*, 2017, **27**, 1604262.
26 P. Bai, G. Zhu, Y. S. Zhou, S. Wang, J. Ma, G. Zhang and Z. L. Wang, *Nano Res.*, 2014, **7**, 990–997.
27 K. Y. Lee, S. K. Kim, J.-H. Lee, D. Seol, M. K. Gupta, Y. Kim and S.-W. Kim, *Adv. Funct. Mater.*, 2016, **26**, 3067–3073.
28 J. I. Scheinbeim, *J. Appl. Phys.*, 1981, **52**, 5939–5942.
29 J. I. Scheinbeim, J. W. Lee and B. A. Newman, *Macromolecules*, 1992, **25**, 3729–3732.
30 S. L. Wu, J. I. Scheinbeim and B. A. Newman, *J. Polym. Sci., Part B: Polym. Phys.*, 1999, **37**, 2737–2746.
31 H. Isoda and Y. Furukawa, *J. Phys. Chem. B*, 2015, **119**, 14309–14314.
32 Q. Zhang, Z. Mo, H. Zhang, S. Liu and S. Z. D. Cheng, *Polymer*, 2001, **42**, 5543–5547.
33 Z. Zhang, M. H. Litt and L. Zhu, *Macromolecules*, 2016, **49**, 3070–3082.
34 S. S. Nair, C. Ramesh and K. Tashiro, *Macromolecules*, 2006, **39**, 2841–2848.
35 K. Meurisch, B. Gojdka, T. Strunskus, V. Zaporojtchenko and F. Faupel, *J. Phys. D: Appl. Phys.*, 2012, **45**, 55304.
36 M. Dhanalakshmi and J. P. Jog, *eXPRESS Polym. Lett.*, 2008, **2**, 540–545.
37 S.-L. Wu, J. I. Scheinbeim and B. A. Newman, *J. Polym. Sci., Part B: Polym. Phys.*, 1996, **34**, 3035–3053.
38 G. Mago, D. M. Kalyon and F. T. Fisher, *J. Polym. Sci., Part B: Polym. Phys.*, 2011, **49**, 1311–1321.

39 Z. Hu, M. Tian, B. Nysten and A. M. Jonas, *Nat. Mater.*, 2009, **8**, 62–67.
40 M. C. García-Gutiérrez, A. Linares, J. J. Hernández, D. R. Rueda, T. A. Ezquerra, P. Poza and R. J. Davies, *Nano Lett.*, 2010, **10**, 1472–1476.
41 R. A. Whiter, V. Narayan and S. Kar-Narayan, *Adv. Energy Mater.*, 2014, **4**, 1400519.
42 Y. Calahorra, R. A. Whiter, Q. Jing, V. Narayan and S. Kar-Narayan, *APL Mater.*, 2016, **4**, 116106.
43 M. Steinhart, P. Göring, H. Dernaika, M. Prabhukaran, U. Gösele, E. Hempel and T. Thurn-Albrecht, *Phys. Rev. Lett.*, 2006, **97**, 1–4.
44 J. Pepin, V. Miri and J. M. Lefebvre, *Macromolecules*, 2016, **49**, 564–573.
45 P. Frübing, A. Kremmer, R. Gerhard-Multhaupt, A. Spanoudaki and P. Pissis, *J. Chem. Phys.*, 2006, **125**, 214701.
46 C. L. Jackson and G. B. McKenna, *J. Chem. Phys.*, 1990, **93**, 9002.
47 L. H. A. S. L. Lai, J. Y. Guo, V. Petrova and G. Ramanath, *Phys. Rev. Lett.*, 1996, **77**, 99–102.
48 Q. Zhang, Z. Mo, S. Liu and H. Zhang, *Macromolecules*, 2000, **33**, 5999–6005.
49 H. H. Yu and L. J. Fina, *Macromolecules*, 1994, **27**, 6192–6200.
50 J. Jakeš and S. Krimm, *Spectrochim. Acta, Part A*, 1971, **27**, 19–34.